Control of brain network dynamics across diverse scales of space and time

Evelyn Tang, ^{1,2} Harang Ju, ^{1,3} Graham L. Baum, ^{1,3} David R. Roalf, ⁴ Theodore D. Satterthwaite, ⁴ Fabio Pasqualetti, ⁵ and Danielle S. Bassett ^{1,4,6,7,8,9}

¹Department of Bioengineering, School of Engineering & Applied Science, University of Pennsylvania, Pennsylvania 19104, USA

²Max Planck Institute for Dynamics and Self-Organization, Göttingen 37079, Germany

³Neuroscience Graduate Program, Perelman School of Medicine, University of Pennsylvania, Pennsylvania 19104, USA
 ⁴Department of Psychiatry, Perelman School of Medicine, University of Pennsylvania, Pennsylvania 19104, USA
 ⁵Department of Mechanical Engineering, University of California, Riverside, Riverside, California 92521, USA
 ⁶Department of Physics & Astronomy, College of Arts & Sciences, University of Pennsylvania, Pennsylvania 19104, USA
 ⁷Department of Electrical & Systems Engineering, School of Engineering & Applied Science, University of Pennsylvania, Pennsylvania 19104, USA

⁸Department of Neurology, Perelman School of Medicine, University of Pennsylvania, Pennsylvania 19104, USA

⁹Santa Fe Institute, Santa Fe, New Mexico 87501, USA



(Received 18 January 2019; revised manuscript received 31 January 2020; accepted 12 March 2020; published 1 June 2020)

The human brain is composed of distinct regions that are each associated with particular functions and distinct propensities for the control of neural dynamics. However, the relation between these functions and control profiles is poorly understood, as is the variation in this relation across diverse scales of space and time. Here we probe the relation between control and dynamics in brain networks constructed from diffusion tensor imaging data in a large community sample of young adults. Specifically, we probe the control properties of each brain region and investigate their relationship with dynamics across various spatial scales using the Laplacian eigenspectrum. In addition, through analysis of regional modal controllability and partitioning of modes, we determine whether the associated dynamics are fast or slow, as well as whether they are alternating or monotone. We find that brain regions that facilitate the control of energetically easy transitions are associated with activity on short length scales and slow timescales. Conversely, brain regions that facilitate control of difficult transitions are associated with activity on long length scales and fast timescales. Built on linear dynamical models, our results offer parsimonious explanations for the activity propagation and network control profiles supported by regions of differing neuroanatomical structure.

DOI: 10.1103/PhysRevE.101.062301

I. INTRODUCTION

The brain is an inherently networked system that displays incredibly rich and complex dynamics [1,2]. Building accurate models of those dynamics remains a key challenge that is fundamental to the field of neuroscience, with the potential to inform personalized medicine by predicting a patient's disease progression and response to therapy [3–6]. Efforts to build such models necessarily depend on the development of interdisciplinary approaches informed by dynamical systems theory, statistical physics, and network science as well as substantial knowledge of the intricacies of the underlying biology [7]. Because of the multiscale nature of the system [8,9], there are some regimes of function or modalities of measurement whose dynamics are well-fit by one mathematical model and others whose dynamics are well-fit by another mathematical model [2,10–12]. On the one hand, large-scale measurements of brain activity can display a wave-like nature and other characteristics consistent with linear, diffusive dynamics instantiated on a physically embedded system [13–17]. On the other hand, fine timescale measurements of brain activity can display oscillatory characteristics consistent with nonlinear, synchronization dynamics thought to support distributed communication and computation [18–21].

Evidence for the first type of dynamics comes, for example, from studies of both large- and small-scale neuronal processes whose intrinsic or endogeneous activity can be partially explained by simple linear models [13,14]. Moreover, wavelike activity has been observed using functional magentic resonance imaging (fMRI) in the visual cortex, where traveling wave responses to visual stimuli are observed to propagate out from the fovea [16]. Notably, such traveling waves with various timescales have been observed across different regions of the brain [22], and it has been posited that the direction and wavelength of the wave could encode information transmitted between regions [23]. In addition to the outward propagation of activity, spiral waves also occur frequently in the neocortex in vivo, both during pharmacologically induced oscillations and during sleeplike states [24], while seizures may manifest as recurrent spiral waves that propagate in the neocortex [17]. Such multiplicity of phenomena motivates the use of dynamical models that emphasize the spatially embedded nature of brain networks [25], and the extended versus transient responses that such an embedding can support [26]. An example is the use of finite-element modeling to simulate the propagation of brain stimulation [27,28], where effects are distributed on a localized part of brain tissue [29]. Another example is

that of diffusive models, where network diffusion over long timescales has been used to model disease progression in the brain for dementia [15] or to predict longitudinal patterns of atrophy and metabolism in Alzheimer's disease [30].

Evidence for the second type of dynamics comes from studies of both large- and small-scale ensembles that produce rhythmic or oscillatory activity [18,19,31]. For example, scalp electrodes in humans can be used to measure rhythms of certain frequencies, which in turn have been associated with different cognitive processes and behavioral responses [20,21]. For example, attentional control via the inhibition of behaviorally irrelevant stimuli and motor responses has been associated with the synchronization of α and β rhythms between right inferior frontal and primary sensory neocortex [32]. Similarly, higher frequency γ rhythms in local synchronization have been observed during visual responses, while lower frequency β rhythms reflecting coherence over parietal and temporal cortices have been observed during activities that required more multimodal sensory integration [33]. Initial efforts sought to explain such phenomena using a simple neuronal model with conduction delays, where excitatory units describe pyramidal cells and inhibitory units describe interneurons [34]. More recent work suggests that the β rhythms specifically can emerge from the integration of nearly synchronous bursts of excitatory synaptic drive targeting proximal and distal dendrites of pyramidal neurons, where the defining feature of a β event was a strong distal drive to supragranular and infragranular layers of cortex that lasted one β period [35]. Notably, the laminar architecture of the neocortical network has also proven critical for explaining γ rhythms [36].

Although empirical studies find pervasive evidence of these two distinct types of dynamics, the field lacks a complete theoretical framework to model how the spatiotemporal characteristics of these dynamics can inform the control properties of specific brain regions, which are interconnected by a fixed structural network. To address this question, recent efforts have begun to study how such distinct dynamics can be guided or controlled by local energy input [40]. For the control of those features of the dynamics that are well-approximated by linear systems theory, efforts have stipulated a linear model of the dynamics dependent upon the structural network implicit in white matter connectivity [41,42]. This framework of network control has been useful to understand brain anatomy and regional function across multiple species including the nematode Caenorhabditis elegans [43], the fly Drosophila [44], the mouse [44], the macaque [41], and the human [39]. Network control theory has also been used to explore the control profiles of brain regions based on their network connectivity [45], and hence to map control propensities on to canonically understood cognitive functions [39,41,46] and their alterations in psychiatric disorders [47]. For the control of those features of the dynamics that require nonlinear systems theory, network control is more difficult [37,48], but some initial work has begun to assess the utility of control principles for seizure abatement [42] and to determine routes along which information can be propagated by transient synchrony [20,21]. In extending these ongoing efforts, a key challenge remains to build models that can predict not only the generic control properties of a system, but also the length scales over which

control-induced dynamics will propagate, and to link these length scales to the timescales of dynamical transitions or control of activity enacted by regional drivers.

Here, we perform initial numerical experiments to address this challenge by relating new developments in the linear control of regional activity in brain networks and their predicted timescales, with the length scales implicit in nonlinear dynamical models of inter-regional synchronization. We use the framework of network control [49] to probe the relation between control and dynamics in brain networks constructed from diffusion tensor imaging data in a young adult subset of the Philadelphia Neurodevelopmental Cohort, a large community-based sample of youth [50,51]. Use of this large sample allows us to probe relations between control and dynamics in an ensemble of brain networks in which control propensities vary extensively [39]. The paper is organized as follows. Following a description of the formalism in Sec. II, we turn in Sec. III to a review of network controllability metrics and their predictions regarding the control profiles of certain brain regions (see the Appendix for details regarding brain network construction from neuroimaging data). In Sec. IV, we consider metrics for the characterization of spatial scales of synchronization in network dynamics [52] and for the control of such synchronization [53]. In Sec. V, we consider metrics for the characterization of temporal scales of control in network dynamics, specifically assessing the role of modal controllers in driving transient versus extended temporal modes of brain activity [45]. In Sec. VI, we compare the relation between control of timescales and control of length scales that we observe in brain networks to those that we observe in networks constructed via the rules of preferential attachment, gaining insight into the dependence of spatiotemporal control on the underlying topology. In Sec. VII, we place our findings within the broader context of empirical results from neuroimaging experiments. We also discuss the implications of our findings for our understanding of how various controllers are associated with distinct types of dynamics, and in turn how distinct dynamics are associated with different regional controllers. We close with a brief discussion of potential future directions.

II. MATHEMATICAL FRAMEWORK

In this section, we describe a formalism for building network models of brain architecture and states, and for studying network controllability of brain dynamics.

A. Network models of brain architecture and states

Here, we study 190 brain networks describing the white matter connectivity of youth in the Philadelphia Neurodevelopmental Cohort. For each network composed of N = 234 cortical and subcortical brain regions, $\mathbf{A} \in \mathbb{R}^{N \times N}$ is a symmetric and weighted adjacency matrix whose elements indicate the number of white matter streamlines connecting two different brain regions indexed with (i, j). For further details regarding the construction of brain networks from neuroimaging data see the Appendix, and for prior work in this data set see Refs. [39,46,54,55].

More formally, a networked system such as the brain can be represented by the graph $\mathcal{G} = (\mathcal{V}, \mathcal{E})$, where \mathcal{V} and \mathcal{E} are

the vertex and edge sets, respectively. Let a_{ij} be the weight associated with the edge $(i, j) \in \mathcal{E}$, and define the weighted adjacency matrix of \mathcal{G} as $A = [a_{ij}]$, where $a_{ij} = 0$ whenever $(i, j) \notin \mathcal{E}$. We associate a real value (state) with each node, collect the node states into a vector (network state), and define the map $x : \mathbb{N}_{\geq 0} \to \mathbb{R}^n$ to describe the evolution (network dynamics) of the network state over time.

Next we seek to define an appropriate equation of state. Based on prior work demonstrating the utility of simple linear models in predicting intrinsic brain dynamics across spatial scales [13,14], we employ a simplified noise-free linear discrete-time and time-invariant network model [41]:

$$\mathbf{x}(t+1) = \mathbf{A}\mathbf{x}(t) + \mathbf{B}_{\mathcal{K}}\mathbf{u}_{\mathcal{K}}(t), \tag{1}$$

where $\mathbf{x}: \mathbb{R}_{\geqslant 0} \to \mathbb{R}^N$ describes the state (i.e., a measure of the electrical charge, oxygen level, or firing rate) of brain regions over time, and $\mathbf{A} \in \mathbb{R}^{N \times N}$ is the structural connectivity described in the previous section. Hence, the size of the vector \mathbf{x} is given by N, and the value of \mathbf{x} describes the brain activity of that region.

B. Network controllability of brain dynamics

To assess controllability of this networked system, we must first ensure its stability and define input points for the injection of control energy. We note first that the diagonal elements of the matrix **A** satisfy $A_{ii} = 0$. Next we note that to assure Schur stability, we divide the matrix by $1 + \xi_0(\mathbf{A})$, where $\xi_0(\mathbf{A})$ is the largest eigenvalue of **A**. The input matrix $\mathbf{B}_{\mathcal{K}}$ identifies the control points \mathcal{K} in the brain, where $\mathcal{K} = \{k_1, \dots, k_m\}$ and

$$B_{\mathcal{K}} = [e_{k_1} \cdots e_{k_m}], \tag{2}$$

and e_i denotes the *i*th canonical vector of dimension N. The input $\mathbf{u}_{\mathcal{K}}: \mathbb{N} \to \mathbb{R}^{|\mathcal{K}|}$ denotes the control strategy, i.e., the control signal injected into the network via the nodes \mathcal{K} . More precisely, it is a map from the set of natural numbers (representing the time instant), and the set of real vectors of length $|\mathcal{K}|$ (representing the actual control vector).

We can now study the *controllability* of this dynamical system, which refers to the possibility of driving the state of the system to a specific target state by means of an external control input [56]. Classic results in control theory ensure that controllability of the network Eq. (1) from the set of nodes $\mathcal K$ is equivalent to the controllability Gramian $\mathbf W_{\mathcal K}$ being invertible, where

$$\mathbf{W}_{\mathcal{K}} = \sum_{\tau=0}^{\infty} \mathbf{A}^{\tau} \mathbf{B}_{\mathcal{K}} \mathbf{B}_{\mathcal{K}}^{\mathsf{T}} \mathbf{A}^{\tau}. \tag{3}$$

Consistent with Refs. [39,41,46,47], we use this framework to choose control nodes one at a time, and thus the input matrix $\mathbf{B}_{\mathcal{K}}$ in fact reduces to a one-dimensional vector, e.g., $\mathbf{B}_{\mathcal{K}} = \begin{pmatrix} 1 & 0 & 0 & \cdots \end{pmatrix}^T$ when the first brain region is the control node. In this case, \mathcal{K} simply describes this control node, i.e., the controllability Gramian can be indexed by the *i*th control node that it describes: \mathbf{W}_i .

III. CONTROLLABILITY METRICS FOR BRAIN NETWORKS

Within the network controllability framework, we study two different control strategies that describe the ability to move the network into different states defined as patterns of regional activity. While the brain certainly displays nonlinear activity, we study a linear model of this more complex nonlinear process which is valid in a neighborhood of the linearization point [see Fig. 1(a)]. Modeling of brain activity in large-scale regional networks shows that the linear approximation provides fair explanatory power of resting state fMRI BOLD data [13]. Further, studies of this controllability framework using nonlinear oscillators connected with coupling constants estimated from white matter tracts shows a good overlap with the linear approximation [37].

The energy landscape of the linear model is quadratic, with at most one energy minimum (at the origin), corresponding to the only state that can be maintained without cost. Note that this origin of the linear system corresponds to the linearization point, i.e., the equilibrium configuration of the nonlinear model from which the linear model is obtained. Using the linear model described in the previous section, we can introduce two controllability metrics. Intuitively, average controllability describes the ease of transition to many states nearby on an energy landscape, while modal controllability describes the ease of transition to a state distant on this landscape [see Fig. 1(a)].

Average controllability of a network equals the average input energy from a set of control nodes and over all possible target states. As a known result, average input energy is proportional to $\mathrm{Trace}(\mathbf{W}_{\mathcal{K}}^{-1})$, the trace of the inverse of the controllability Gramian. Instead and consistent with Refs. [39,41,46], we adopt Trace($\mathbf{W}_{\mathcal{K}}$) as a measure of average controllability for two main reasons: first, Trace(\mathbf{W}_{κ}^{-1}) and $Trace(\mathbf{W}_{\mathcal{K}})$ satisfy a relation of inverse proportionality, so that the information obtained from the two metrics are correlated with one another and, second, $\mathbf{W}_{\mathcal{K}}$ is typically very ill-conditioned even for coarse network resolutions, so that $\operatorname{Trace}(\mathbf{W}_{\kappa}^{-1})$ cannot be accurately computed even for small brain networks. It should be noted that Trace($\mathbf{W}_{\mathcal{K}}$) encodes a well-defined control metric, namely the energy of the network impulse response or, equivalently, the network H_2 norm [57]. As discussed above, when a brain region i serves as a control node, the resulting Gramian can be indexed as W_i , in order to compute the regional average controllability.

To calculate the trace of the Gramian, we avoid the numerical difficulties associated with solving the Lyapunov equation [58–61]. Given the stability of our matrix **A**, we can use the following:

$$\begin{aligned} \operatorname{Trace}(\mathbf{W}_{\mathcal{K}}) &= \operatorname{Trace}\left(\sum_{\tau=0}^{\infty} \mathbf{A}^{\tau} \mathbf{B}_{\mathcal{K}} \mathbf{B}_{\mathcal{K}}^{\mathsf{T}} \mathbf{A}^{\tau}\right) \\ &= \sum_{\tau=0}^{\infty} \operatorname{Trace}(\mathbf{A}^{\tau} \mathbf{B}_{\mathcal{K}} \mathbf{B}_{\mathcal{K}}^{\mathsf{T}} \mathbf{A}^{\tau}) \\ &= \sum_{\tau=0}^{\infty} \operatorname{Trace}(\mathbf{A}^{2\tau} \mathbf{B}_{\mathcal{K}} \mathbf{B}_{\mathcal{K}}^{\mathsf{T}}) \\ &= \left(\sum_{\tau=0}^{\infty} \mathbf{A}^{2\tau}\right) (\mathbf{B}_{\mathcal{K}} \mathbf{B}_{\mathcal{K}}^{\mathsf{T}}) \\ &= (\mathbf{I} - \mathbf{A}^{2\tau})^{-1} (\mathbf{B}_{\mathcal{K}} \mathbf{B}_{\mathcal{K}}^{\mathsf{T}}). \end{aligned}$$

Here we used some properties of our system, that \mathcal{K} contains only one node and \mathbf{A} is symmetric.

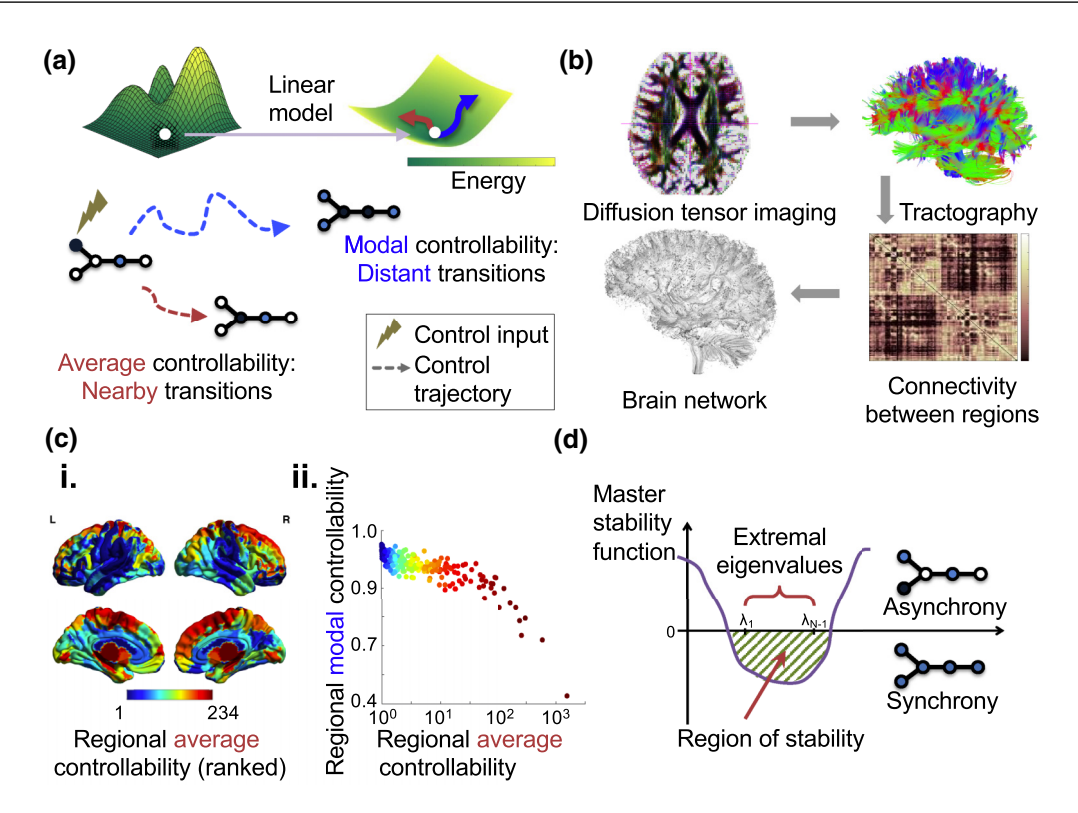


FIG. 1. Controllability and synchronizability in brain networks. (a) While the brain displays nonlinear dynamics (top left), linear models (top right) have shown great utility in predicting such dynamics across spatial scales [13,14,37]. We study two such metrics: Average controllability provides an intuitive measure of the structural support for moving the brain to easy-to-reach states (short red transition), whereas modal controllability provides an intuitive measure of the structural support for moving the brain to difficult-to-reach states (long blue transition). (b) Diffusion tensor imaging measures the direction of water diffusion in the brain. From this data, white matter streamlines can be reconstructed that connect brain regions in a structural network. (c.i) Regional average controllability ranked on N = 234 brain regions of a group-averaged network for visualization purposes. (c.ii) Regions with high average controllability tend to display low modal controllability: $\rho = -0.76$, df = 233, $p < 1 \times 10^{-16}$. (d) We operationalize a synchronous state as a state in which all nodes have the same activity magnitude. Such a state is stable when the master stability function is negative for all positive eigenvalues of the graph Laplacian [38]. Following Ref. [39], we use the inverse spread of the Laplacian eigenvalues $1/\sigma^2(\{\lambda_i\})$ as a measure of global synchronizability. Adapted with permission from Ref. [39].

Modal controllability refers to the ability of a node to control each time-evolving mode of a dynamical network and can be used to identify states that are difficult to control from a set of control nodes. Modal controllability is computed from the eigenvector matrix $V = [v_{ij}]$ of the network adjacency matrix A. By extension from the PBH test [57], if the entry v_{ij} is small, then the jth mode is poorly controllable from node i. Following Ref. [45], we define

$$\phi_i = \sum_{j} \left[1 - \xi_j^2(A) \right] v_{ij}^2 \tag{4}$$

as a scaled measure of the controllability of all N modes $\xi_0(\mathbf{A}), \ldots, \xi_{N-1}(\mathbf{A})$ from the brain region i, allowing the computation of regional modal controllability. Regions with high modal controllability are able to control all of the dynamic modes of the network and hence to drive the dynamics toward hard-to-reach configurations.

We study these metrics in the 190 structural brain networks derived from diffusion tensor imaging data [see Fig. 1(b)]. On a group-representative brain network constructed by averaging all 190 subject-specific networks, we calculate these controllability metrics and show their distribution across the brain [see Fig. 1(c.i)]. Consistent with prior work in both

this and other data sets [39,41], we find that regions with high average controllability tend to be located in network hubs associated with the default-mode system, a set of regions that tend to be active during intrinsic processing. Interestingly and again consistent with prior work in this and other data sets [39,41,47,62], regions with high modal controllability tend to display low average controllability [see Fig. 1(c.ii)], and are predominantly found in regions of the brain that become active during tasks that demand high levels of executive function or cognitive control.

IV. CONTROLLABILITY OF SPATIAL SCALES: NETWORK DYNAMICS IN HARMONIC WAVES

In contrast to the time-varying or transient dynamics that can be described using models mentioned in the previous section, recent observations of brain dynamics also include sustained patterns of collective activity across relatively large areas [22,63]. Such wave patterns call for a different description: one better suited by a framework developed for networked oscillators and synchronized activity.

Specifically, the previous linear model [Eq. (1)] is not relevant to wavelike dynamics, even as it is supported by

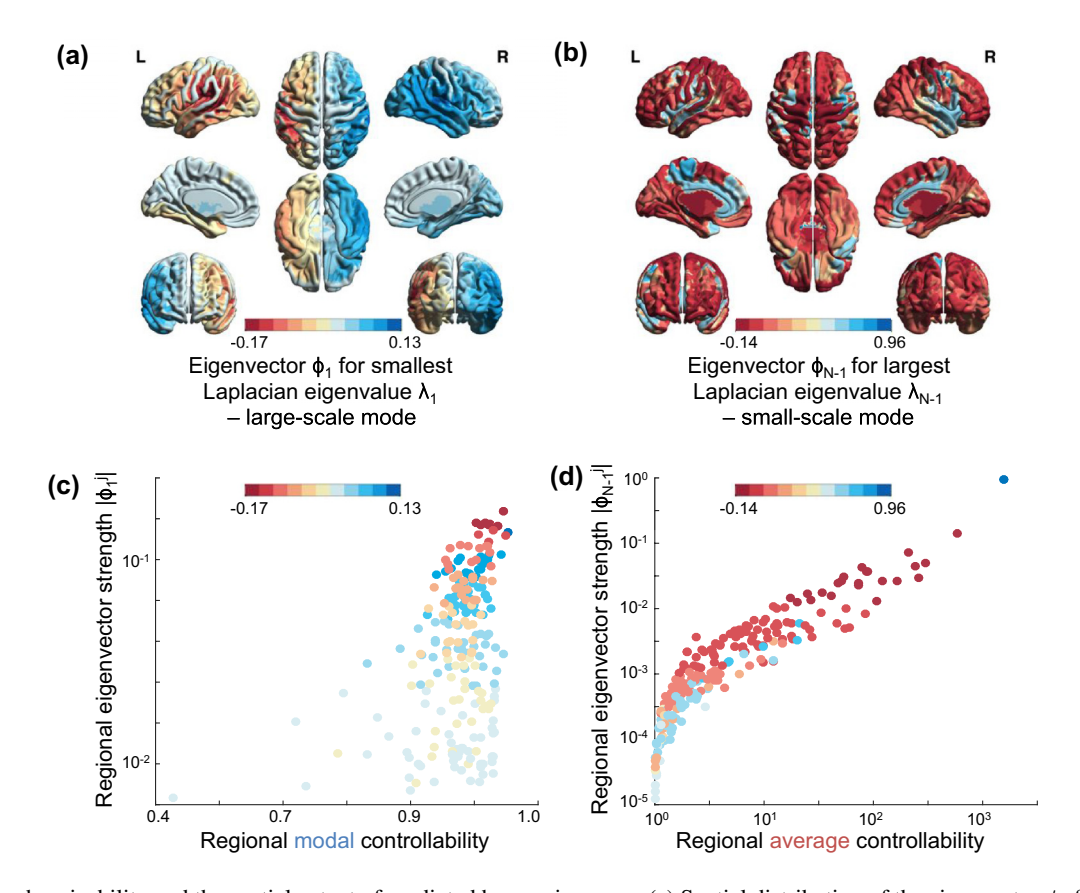


FIG. 2. Synchronizability and the spatial extent of predicted harmonic waves. (a) Spatial distribution of the eigenvector ϕ_1 for the smallest Laplacian eigenvalue λ_1 , showing which regions on a group-averaged brain network most strongly contribute to this large-scale mode. (b) Spatial distribution of the eigenvector ϕ_{N-1} for the largest Laplacian eigenvalue λ_{N-1} , showing which regions most strongly contribute to this small-scale mode. (c) Regions most relevant for this large-scale mode $|\phi_1^j|$ are positively correlated with regions of high modal controllability: $\rho = 0.27$, df = 233, $p < 1 \times 10^{-4}$. (d) Regions most relevant for this small-scale mode $|\phi_{N-1}^j|$ are positively correlated with regions of high average controllability: $\rho = 0.95$, df = 233, $p < 1 \times 10^{-5}$. Note that the color in panels (a, b) is recapitulated by values along the vertical axis in panels (c, d), simply for ease of identifying relevant brain regions with the given results.

other empirical observations [13,14,43]. Therefore, to complement our previous efforts to study the control of brain state transitions via a simple linear model of network dynamics, here we turn to the question of how to control the synchrony of harmonic waves [52] which naturally arise in the same underlying white matter architecture. Notably, extensive prior work in the dynamical systems literature has considered ways in which to measure the synchronizability of a networked system. To be clear, here we define the synchronizability as a measure of the ability of a network to persist in a single synchronous state $\mathbf{s}(t)$, i.e., $\mathbf{x}_1(t) = \dots = \mathbf{x}_n(t+1) = \mathbf{s}(t)$. The master stability function (MSF) allows analysis of the stability of this synchronous state without detailed specification of the properties of the dynamical units [see Fig. 1(d)] [38]. Within this framework, linear stability depends upon the positive eigenvalues $\{\lambda_i\}$, i = 1, ..., N - 1 of the Laplacian matrix Ldefined by $L_{ij} = \delta_{ij} \sum_{k} A_{ik} - A_{ij}$. The synchronous state is stable when the master stability function is negative for all positive eigenvalues of the graph Laplacian [see Fig. 1(d)].

For the purposes of control, it is useful to note that the structure of the graph Laplacian provides information regarding the most likely modes of standing waves: the vibrational states of a dynamical system in which the frequency of vibration is the same for all elements. These modes are given

by the eigenvectors of the graph Laplacian. For example, the eigenvector ϕ_1 of the smallest positive Laplacian eigenvalue λ_1 is an odd mode associated with large-scale waves [38,52] [Fig. 2(a)]. In contrast, the eigenvector ϕ_{N-1} of the largest Laplacian eigenvalue λ_{N-1} is an even mode associated with small-scale waves [Fig. 2(b)]. Recent developments in pushpull control capitalize on these relations to control the transition into and out of synchrony by targeting network nodes that have a large weight for a given extremal eigenvector of the Laplacian [53].

To investigate the control of synchrony in the harmonic waves of brain networks, we calculate the eigenvectors of the Laplacian for each subject, and then we average the eigenvectors across all of the 190 subjects. We observe that the strength of control for harmonic waves of a network can be understood in terms of the network's predisposition to average and modal control. First, we observe that the regional strength of the large-scale waves $|\phi_1^j|$ is positively correlated with regional modal controllability [Spearman correlation coefficient $\rho = 0.27$, df = 233, $p < 1 \times 10^{-4}$; Fig. 2(c)]. This relation suggests that regions that enable synchronous behavior over long distances are also predicted to be effective in moving the brain to energetically distant states (see a list of the highest and lowest such regions in Table I of the

Appendix). Second, we observe that the regional strength of the small-scale waves $|\phi_{N-1}^j|$ is positively correlated with regional average controllability [Spearman correlation coefficient $\rho = 0.95$, df = 233, $p < 1 \times 10^{-5}$; Fig. 2(d)]. This relation suggests that regions that enable synchronous behavior over short distances are also predicted to be effective in moving the brain to energetically nearby states (see a list of the highest and lowest such regions in Table II of the Appendix). To confirm that our results do not depend on the stage at which we average over subjects, we also calculate these correlations for the Laplacian spectra obtained from a group-averaged network (procedure described in Sec. II). We find that the regional strength of the large-scale waves in the group network is still positively correlated with regional modal controllability (Spearman correlation coefficient ρ = 0.28, df = 233, $p < 1 \times 10^{-4}$), while the regional strength of the small-scale waves in the group network is still positively correlated with regional average controllability (Spearman correlation coefficient $\rho = 0.86$, df = 233, $p < 1 \times 10^{-5}$). These results demonstrate that our findings do not depend unduly on the stage at which we average over subjects.

V. CONTROLLABILITY OF TEMPORAL SCALES: NETWORK DYNAMICS IN FAST OR SLOW, ALTERNATING OR MONOTONE MODES

To complement the findings reported in the previous section explicating the spatial scales of control, we next turn to a consideration of the timescales of control. We note that in a discrete-time system, the eigenvalues of the network adjacency matrix A give the rate of decay of the various supported modes of activity. These modes of a linear time-invariant system are the elementary components of the dynamic response of the system to stimuli. Each mode gives rise to an elementary response (or trajectory), and the combination of the modes generates more complex responses and trajectories. Distinct processes and timescales of activity are observed in the brain, where rhythms of certain frequencies have been associated with different cognitive processes and behavioral responses [20,21]. For instance, higher frequency γ rhythms in local synchronization emerge during visual responses, while lower frequency β rhythms reflecting coherence over parietal and temporal cortices have been observed during activities that required more multimodal sensory integration [33,35]. In our discrete time linear model, the eigenvalues with large magnitude decay slowly while the eigenvalues with small magnitude decay quickly. The relationship between eigenvalues and the rate of decay of associated modes of activity suggests that the control of such modes can be analyzed separately for different timescales. Although our prior expression for modal controllability [Eq. (4)] summed over all Nmodes of the adjacency matrix A, we can instead partition the sum into different groups based on the eigenvalues ξ_i of the modes. For instance, a region i can be evaluated for its controllability of fast modes with $\phi_i^{\text{fast}} = \sum_j^{\text{small}} \frac{|\xi_j|}{v_{ij}^2} \frac{v_{ij}^2}{\text{and for}}$ its controllability of slow modes with $\phi_i^{
m slow} = \sum_j^{|{
m large}\>|k_j|} v_{ij}^2$ Note that in this case, all the eigenvalues have magnitude smaller than 1. Further, in the above expression we have also removed the scaling factor in Eq. (4) of $[1 - \xi_i^2(A)]$ as this factor is unnecessary for the calculation of control timescales;

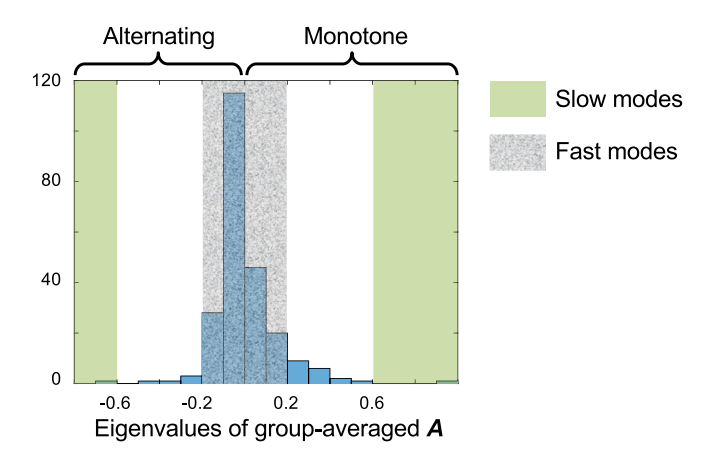


FIG. 3. Extracting fast or slow, and alternating or monotone modes of network dynamics. Here we show the histogram of N=234 eigenvalues of the group representative brain network, constructed by averaging all 190 subject-specific brain networks. Given the trimodal distribution of eigenvalues, we partition them into a densely populated cluster of $|\xi_j| < 0.2$, a lightly populated cluster of $0.2 < |\xi_j| < 0.6$, and the remaining $|\xi_j| > 0.6$ eigenvalues that are separated from the other modes with a clear gap. This partitioning can be done for both positive and negative eigenvalues, respectively, which correspond to the monotone and alternating modes of the system. From left to right, these groups are $\xi_j < -0.6$ (slow alternating), $-0.2 < \xi_j < 0$ (fast alternating), $0 < \xi_j < 0.2$ (fast monotone), and $\xi_j > 0.6$ (slow monotone), respectively.

in supporting calculations, we also verified that the inclusion or exclusion of this factor does not alter our subsequent findings.

To investigate regional propensities for the control of fast versus slow modes, we considered the group-representative network constructed by averaging all 190 subject-specific brain networks. We examined the spectrum of this representative network (see Fig. 3), and note that there are three well-separated groups of eigenvalues. In the center, there is a densely populated cluster of magnitude between 0 and 0.2 (fast), which have at least double the modes in each bin of width 0.1 as compared to all the bins outside this cluster. On the two ends, there are sparse modes with magnitude above 0.6 (slow) that have a clear gap from all the other modes. In between these above mentioned groups, there is a lightly populated cluster of eigenvalue magnitude between 0.2 and 0.6, which are distinct from the other groups due to the reasons mentioned. Given this visually trimodal distribution, it is hence natural to partition the eigenvalues into three groups that differ in their relevant timescales: $|\xi_i| < 0.2$ (fast), 0.2 < $|\xi_i| < 0.6$ (medium), and $|\xi_i| > 0.6$ (slow).

Now, it is also important to note that eigenvalues carry additional information: the sign of the eigenvalue determines the nature of the system's response, where a mode with a positive eigenvalue decays monotonically with each time step, while a mode with a negative eigenvalue has a decaying response that alternates between positive and negative values at each time step. To allow sensitivity to these monotone and alternating modes, we can restrict the range in the sum of $\phi_i^{\rm fast}$ and $\phi_i^{\rm slow}$ to the positive or to the negative eigenvalues. By doing so, we now have four groups of interest: $0 < \xi_i < 0.2$ (fast

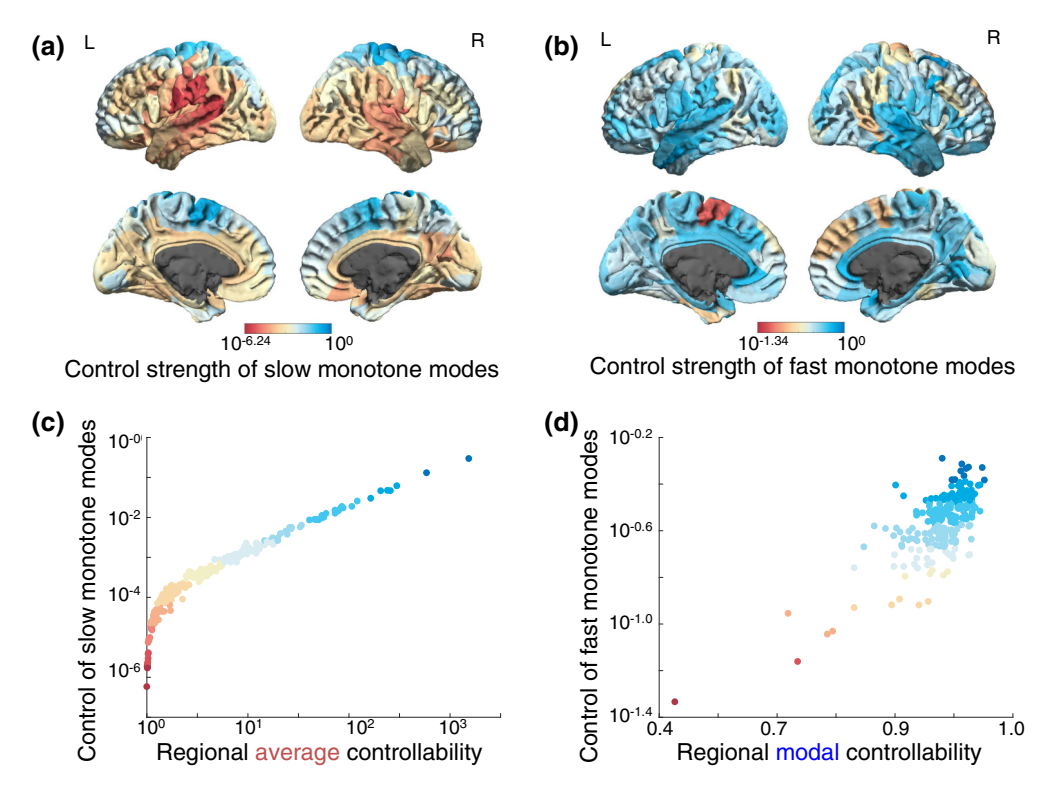


FIG. 4. Monotone modes and their control profiles across the brain. (a) Spatial distribution of the controllability of slow monotone modes ($\xi_j > 0.6$), showing which regions on a group-representative brain network most strongly contribute. (b) Spatial distribution of the controllability of fast monotone modes ($0 < \xi_j < 0.2$), showing which regions on a group-representative network most strongly contribute. (c) Regions most relevant for control of slow monotone modes tended to be regions of high average controllability: $\rho = 0.99$, df = 233, $p < 1 \times 10^{-4}$. (d) Regions most relevant for control of fast monotone modes tended to be regions of high modal controllability: $\rho = 0.59$, df = 233, $p < 1 \times 10^{-4}$. Note that the color in panels (a, b) is recapitulated by values along the vertical axis in panels (c, d), simply for ease of identifying relevant brain regions with the given results.

monotone), $\xi_j > 0.6$ (slow monotone), $-0.2 < \xi_j < 0$ (fast alternating), and $\xi_j < -0.6$ (slow alternating). By separately identifying these diverse modes, we can determine whether and how brain regions' differing controllability of particular timescales might relate to their differing controllability of various length scale modes.

Beginning with the control of only monotone dynamics, we find that support for slow monotone dynamics (eigenvalues $\xi_i > 0.6$) differs across the brain with greatest support located in the prefrontal cortex and temporoparietal junction [Fig. 4(a); see a list of the highest and lowest such regions in Table III of the Appendix]. Moreover, we find that the degree to which a regional controller supports slow monotone dynamics is strongly and positively correlated with regional average controllability [Spearman correlation coefficient ρ = 0.99, df = 233, $p < 1 \times 10^{-4}$; Fig. 4(c)], providing support for energetically easy state transitions. Similarly, we also find that support for fast monotone dynamics (eigenvalues $0 < \xi_i < 0.2$) differs across the brain with greatest support located in subcortical areas [Fig. 4(b); see a list of the highest and lowest such regions in Table IV of the Appendix]. In addition, we find that the degree to which a regional controller supports fast monotone dynamics is strongly and positively correlated with regional modal controllability [ρ = 0.59, df = 233, $p < 1 \times 10^{-4}$; Fig. 4(d)], providing support for energetically more difficult state transitions.

When studying the control of alternating dynamics, we find that support for slow alternating dynamics (eigenvalues ξ_i < -0.6) differs across the brain with greatest support located in the temporoparietal junction, inferior frontal gyrus, and precuneus [Fig. 5(a); see a list of the highest and lowest such regions in Table V of the Appendix]. Moreover, we find that the degree to which a regional controller supports slow alternating dynamics is strongly and positively correlated with regional average controllability [$\rho = 0.83$, df =233, $p < 1 \times 10^{-4}$; Fig. 5(c)], providing support for energetically easy state transitions. Last, we also find that support for fast alternating dynamics (eigenvalues $-0.2 < \xi_i <$ 0) differs across the brain with greatest support located in several midline structures [Fig. 5(b); see a list of the highest and lowest such regions in Table VI of the Appendix]. In this case, we find that the degree to which a regional controller supports fast alternating dynamics is strongly and positively correlated with regional modal controllability $[\rho =$ 0.24, df = 233, $p < 2 \times 10^{-4}$; Fig. 5(d)], providing support for energetically more difficult state transitions.

VI. DEPENDENCE UPON GRAPH ARCHITECTURE

The results described thus far provide striking relations between the temporal and spatial scales of network dynamics that a brain region can control. An interesting and important

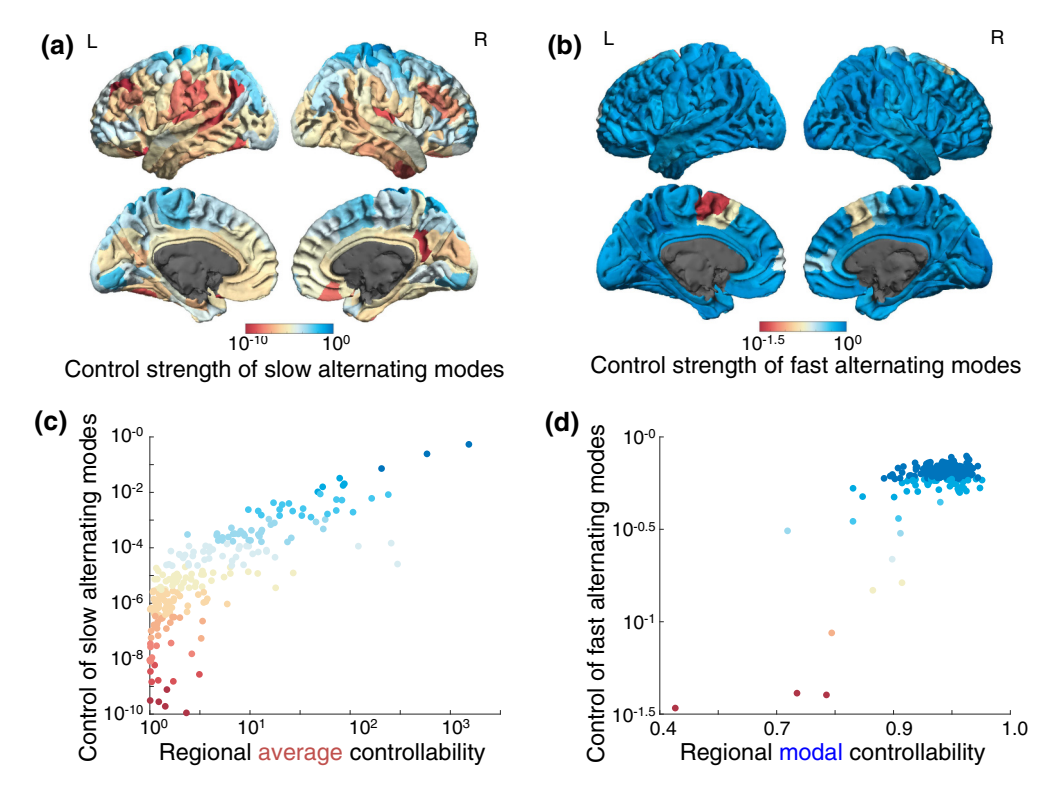


FIG. 5. Alternating modes and their control profiles across the brain. (a) Spatial distribution of the controllability of slow alternating modes ($\xi_j < -0.6$), showing which regions on a group-representative brain network most strongly contribute. (b) Spatial distribution of the controllability of fast alternating modes ($-0.2 < \xi_j < 0$), showing which regions on a group-representative network most strongly contribute. (c) Regions most relevant for the control of slow alternating modes tended to be regions of high average controllability: $\rho = 0.83$, df = 233, $p < 1 \times 10^{-4}$. (d) Regions most relevant for the control of fast alternating modes tended to be regions of high modal controllability: $\rho = 0.24$, df = 233, $p < 2 \times 10^{-4}$. Note that the color in panels (a, b) is recapitulated by values along the vertical axis in panels (c, d), simply for ease of identifying relevant brain regions with the given results.

question to ask is whether and to what degree these relations hold true in graph models with vastly different topologies. In choosing a particularly dissimilar comparator, we consider the fact that human brain networks are known to display high clustering and short path length [64,65], community structure [54], and core-periphery structure [66]. A notable graph model that stands in stark contrast to this architecture is the scale-free model [67], also sometimes referred to as the preferential attachment model [68] or the Barabasi-Albert model [69], which displays low clustering and longer path length, less community structure, and less core-periphery structure. For ease of comparison, we provide a table contrasting these primary network metrics in both networks; see Table VII in the Appendix.

We therefore study a synthetically constructed Barabasi-Albert network with the same number of nodes (N=234) and the same average strength as the group-representative brain network in our empirical data set. As before, we calculate controllability metrics and the Laplacian eigenvectors to investigate the spatial harmonics. We find that the relationships between controllers of different length scales with average and modal controllers remain similar across both brain and Barabasi-Albert graphs. Specifically, the nodes in the Barabasi-Albert graph most relevant for the large-scale mode $|\phi_1^j|$ tend to be the nodes with high modal controllability: $\rho=0.64$, df=233, $p<1\times10^{-4}$. Meanwhile, the

nodes in the Barabasi-Albert graph most relevant for the small-scale mode $|\phi_{N-1}^j|$ tend to be the nodes with high average controllability: $\rho=0.77,\ df=233,\ p<1\times10^{-5}.$ Such positive correlations were also found in the brain network (Sec. III).

To study the control of modes with different timescales, we employ the same partition that we used in the brain network, i.e., groups of $|\xi_i| < 0.2$, $0.2 < |\xi_i| < 0.6$, and $|\xi_i| > 0.6$ for both positive and negative eigenvalues, respectively (see Fig. 6). Interestingly, we find that the distribution of eigenvalues differs significantly in the Barabasi-Albert network in comparison to the group-representative brain network, with the striking absence of slow alternating modes. When we consider only the fast alternating modes, we observe that the relationship between the controllers of these fast modes and the modal controllers is inverted in the Barabasi-Albert network in comparison to the group-representative brain network (see Fig. 7). In the brain, the degree to which a regional controller supports fast alternating dynamics tracks the degree to which that same regional controller supports energetically more difficult transitions. In the Barabasi-Albert network, the degree to which a regional controller supports fast alternating dynamics is anti-correlated with the degree to which that same regional controller supports energetically more difficult transitions (Spearman correlation coefficient $\rho = -0.91$, df =233, $p < 1 \times 10^{-4}$).

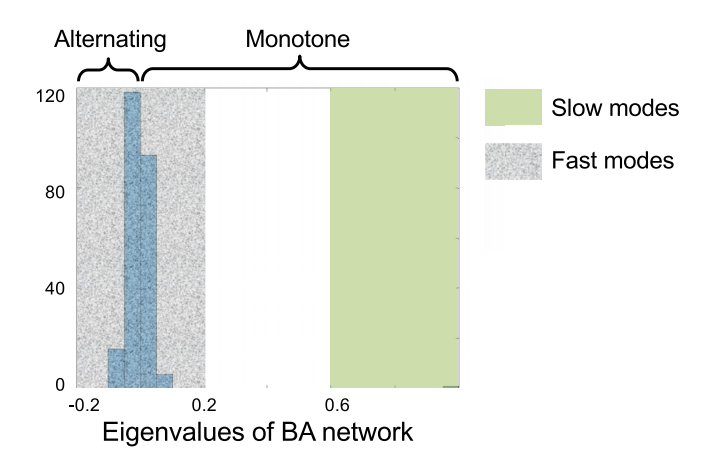


FIG. 6. Histogram of N=234 eigenvalues of a Barabasi-Albert preferential attachment network. As we had done for the group-representative brain network, we make partitions of $|\xi_j| < 0.2$, $0.2 < |\xi_j| < 0.6$, and $|\xi_j| > 0.6$ for positive and negative eigenvalues, respectively, which correspond to the monotone and alternating modes of the system.

VII. DISCUSSION

The human brain displays a variety of different types of dynamics. Here we use two different models to compare the control profiles of various brain regions: diffusion dynamics and network control, respectively. The two dynamical models we use capture different properties of the same brain network, hence it is useful to compare and contrast these different dynamics produced by the same system. The model for synchronizability uses the master stability function (MSF) formalism based on a model of connected oscillators, whereas our controllability analysis relies on a linear discrete time model. Note that while the MSF approach originally studied continuous time systems, there have been extensions to discrete time systems [70]. In the latter case, a modified graph Laplacian is used that has the same eigenvalues as a regular Laplacian operator (and the eigenvectors are similar up to a constant shift) [71]. Hence, our two models are

related by the structure of the network, which appears in the interconnections among the oscillators in the first model, and as a weighted adjacency matrix in the second model. Through these analyses we find that brain regions with high average controllability are also predicted to effectively control dynamics on short length scales, while regions of high modal controllability are predicted to do the converse. In addition, regions of high average controllability are also predicted to effectively control dynamics on slow scales, while regions of high modal controllability are predicted to do the converse. Collectively, our results expand our understanding of the relations between brain network dynamics and control, and the relative roles that different brain regions can play in controlling the diverse length and timescales of neural dynamics.

A. Pertinent theoretical considerations

There are two important theoretical considerations relevant to our work: the relation between linear and nonlinear network control, and the nature of the master stability function. The first consideration is crucial, particularly given recent results regarding the difficulty of applying linear control models to nonlinear systems [72]. While linear models are certainly valid only within the domain of linearization, we note that the modeling of brain activity in large-scale regional networks shows that the linear approximation provides fair explanatory power of resting state fMRI BOLD data [13]. Further, studies of this controllability framework using nonlinear oscillators connected with coupling constants estimated from large-scale white matter structural connections shows a good overlap with the linear approximation [37]. While the model we employ is a discrete-time system, this controllability Gramian is statistically similar to that obtained in a continuous-time system [41], through the comparison of simulations run using MATLAB's lyap function. Regarding the second, we note that we have plotted a typical example of an MSF for a network of oscillators schematically in Fig. 1(d); however, specific details will depend on the dynamics of individual nodes and the connectivity between them. The shape of the MSF

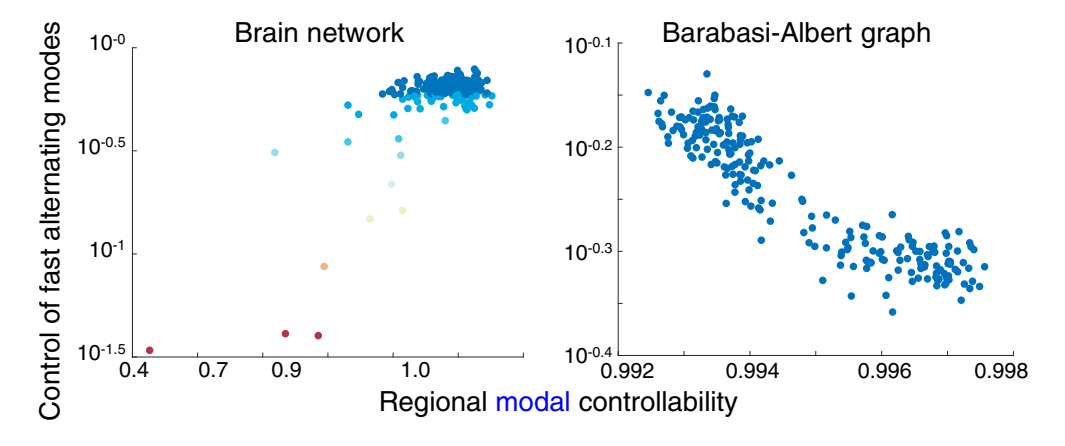


FIG. 7. Different results from the group-representative brain network and a Barabasi-Albert network. Study of the alternating dynamical modes for the two different networks shows that while controllers of fast modes are positively correlated with modal controllers in the brain network (left), the same controllers are negatively correlated in a Barabasi-Albert network (right), $\rho = -0.91$, df = 233, $p < 1 \times 10^{-4}$. [The color in the left image simply corresponds to the strength of control of fast alternating modes, for consistency with Fig. 5(d).]

is typically convex for generic oscillator systems, including chaotic oscillators that have stable limit cycles [73].

Separately, it is worth noting that there are several important and interesting questions at the intersection of control theory and network neuroscience. First, early work focused on the question of whether a brain network is controllable from a single region, providing initial evidence in the affirmative [41]. A subsequent numerical study cast doubt on that evidence [74], while two even later studies provided additional theoretical evidence in the affirmative [75,76]. Notably, the structural controllability of networks depends upon their topology, being quite different for diverse graph models including the Erdős-Rényi, ring lattice, Watts-Strogatz, modular, random geometric, and Barabasi-Albert model [62,75], the latter of which we also study here. Second, several studies address the question of whether a set of control points (network nodes) can be identified that can effectively and reliably induce a particular change in system dynamics [43,77]. Third, another body of work focuses on the question of how to guide the brain from one state of activity to another state of activity given the underlying structural connections along which activity can propagate [78,79]. Work in this vein has offered validated predictions of the effects of brain stimulation [80], and explanations of individual differences in cognitive control [81]. This list of questions is far from exhaustive, and we expand upon it in this work by probing the timescales and spatial scales relevant for control in brain networks.

B. Future directions

Our work provides an initial foray into the combined study of brain network dynamics and control, and how the two depend upon the length scales and timescales of brain states and state transitions. From a mathematical perspective, it would be interesting to study these relations in other graph models with different topologies, and also to work to find analytical forms for the relations we observe in numerical experiments. From a neurophysics perspective, future efforts could extend our work into other age groups, or into clinical groups of patients with psychiatric disease or neurological disorders where such relations might be altered. Efforts could also determine whether our findings in humans are recapitulated in other animals, and across different spatial resolutions of imaging data. Another avenue for further investigation could be the use of directed brain networks, such as those that are available from tract-tracing studies of macaques, which would display complex eigenvalues thereby providing additional oscillatory timescales for more extensive study. Lastly, this trimodal nature of the data (see Fig. 3) appears to arise when studying group-representative data, which led to our choice of timescale bins. Future work could extend our study to the single-subject level, where a distinct and subject-specific binning procedure might prove helpful.

ACKNOWLEDGMENTS

D.S.B. and E.T. acknowledge support from the John D. and Catherine T. MacArthur Foundation, the Alfred P. Sloan Foundation, the ISI Foundation, the Paul G. Allen Family Foundation, the Army Research Laboratory (Grant

No. W911NF-10-2-0022), the Army Research Office (Bassett, Grant No. W911NF-14-1-0679; Grafton, Grants No. W911NF-16-1-0474 and No. DCIST-W911NF-17-2-0181), the Office of Naval Research, the National Institute of Mental Health (Grants No. 2-R01-DC-009209-11, No. R01-MH112847, No. R01-MH107235, and No. R21-M-MH-106799), the National Institute of Child Health and Human Development (Grant No. 1R01HD086888-01), National Institute of Neurological Disorders and Stroke (Grant No. R01NS099348), and the National Science Foundation (Grants No. BCS-1441502, No. BCS-1430087, No. PHY-1554488, and No. BCS-1631550). The content is solely the responsibility of the authors and does not necessarily represent the official views of any of the funding agencies.

APPENDIX

All data were acquired from the Philadelphia Neurodevelopmental Cohort (PNC), a large community-based study of brain development. This resource is publicly available through the Database of Genotypes and Phenotypes. Each subject provided their informed consent according to the Institutional Review Board of the University of Pennsylvania who approved all study protocols. These subjects had no gross radiological abnormalities that distorted brain anatomy, no history of inpatient psychiatric hospitalization, no use of psychotropic medications at the time of scanning, and no medical disorders that could impact brain function. Each included subject also passed both manual and automated quality-assessment protocols for DTI [82] and T1-weighted structural imaging [83], and they had low in-scanner head motion (less than 2 mm mean relative displacement between b = 0 volumes). Here we study a subset of the full group previously reported in Ref. [39]; specifically, we consider the 190 young adults aged 18 to 22 years.

Structural connectivity was estimated using 64-direction DTI data. The diffusion tensor was estimated and deterministic whole-brain fiber tracking was implemented in DSI Studio using a modified FACT algorithm, with exactly one million streamlines initiated per subject after removing all streamlines with length less than 10 mm [41]. A 234-region parcellation [84] was constructed from the T1 image using FreeSurfer. Parcels were dilated by 4 mm to extend regions into white matter, and registered to the first nonweighted (b =0) volume using an affine transform. Edge weights A_{ij} in the adjacency matrix were defined by the number of streamlines connecting each pair of nodes end-to-end. All analyses were replicated using an alternative edge weight definition, where weights are equal to the number of streamlines connecting each node pair divided by the total volume of the node pair, as well as using probabilistic fiber tracking methods. A schematic for structural connectome construction is depicted in Fig. 1(b).

Lastly, we provide identification of the brain regions most relevant for the control of large and small spatial scales, as well as for fast and slow control of different dynamics. The highest and lowest five brain regions in Figs. 2–5 are listed in Tables I–VI.

TABLE I. Brain regions with highest and lowest weights for the largest-scale Laplacian eigenvector [Fig. 2(a)].

Highest	Lowest	
Postcentral 6 (L)	Brainstem (L)	
Supramarginal 2 (L)	Precentral 1 (L)	
Supramarginal 3 (L)	Superior frontal 8 (L)	
Supramarginal 1 (L)	Caudate (L)	
Postcentral 7 (L)	Postcentral 1 (L)	

TABLE II. Brain regions with highest and lowest weights for the smallest-scale Laplacian eigenvector [Fig. 2(b)].

Highest	Lowest
Brainstem (L)	Postcentral 6 (L)
Precentral 6 (R)	Postcentral 7 (L)
Postcentral 5 (R)	Supramarginal 3 (L)
Thalamus proper (R)	Supramarginal 2 (L)
Thalamus proper (L)	Postcentral 1 (R)

TABLE III. Brain regions that provide the highest and lowest support for the control of slow monotone dynamics [Fig. 4(a)].

Highest	Lowest	
Brainstem (L)	Postcentral 6 (L)	
Precentral 6 (R)	Superior temporal 1 (L)	
Thalamus proper (R)	Supramarginal 3 (L)	
Thalamus proper (L)	Banks STS 1 (L)	
Superior frontal 8 (L)	Transverse temporal 1 (R)	

TABLE IV. Brain regions that provide the highest and lowest support for the control of fast monotone dynamics [Fig. 4(b)].

Highest	Lowest
Superior frontal 8 (R)	Brainstem (L)
Middle temporal 4 (L)	Superior frontal 8 (L)
Insula 2 (L)	Thalamus proper (L)
Transverse temporal 1 (L)	Thalamus proper (R)
Superior temporal 2 (R)	Precentral 6 (R)

TABLE V. Brain regions that provide the highest and lowest support for the control of slow alternating dynamics [Fig. 5(a)].

Highest	Lowest	
Brainstem (L)	Rostral middle frontal 2 (L)	
Precentral 6 (R)	Lateral orbitofrontal 1 (L)	
Postcentral 5 (R)	Precuneus 2 (R)	
Precentral 3 (L)	Banks STS 1 (L)	
Precentral 2 (L)	Inferior parietal 3 (L)	

TABLE VI. Brain regions that provide the highest and lowest support for the control of fast alternating dynamics [Fig. 5(b)].

Highest	Lowest	
Lateral occipital 3 (R)	Brainstem (L)	
Lateral occipital 1 (R)	Thalamus proper (L)	
Precuneus 2 (L)	Superior frontal 8 (L)	
Lingual 3 (L)	Thalamus proper (R)	
Accumbens area (L)	Superior frontal 5 (R)	

TABLE VII. We calculate primary network metrics for both the brain network and a Barabasi-Albert graph with the same number of nodes (N = 234) and the same normalization (see Sec. IIB): the metrics of clustering coefficient, characteristic path length, modularity, and coreness, respectively [86]. Uncertainty measurements are standard errors; modularity (a heuristic) is calculated over 1000 trials maximizing a common modularity quality function [87].

	Brain network	Barabasi-Albert graph
Clustering coefficient [85]	$(5.5 \times 10^{-4}) \pm (1.5 \times 10^{-4})$	$(4.3 \times 10^{-3}) \pm (1.3 \times 10^{-5})$
Characteristic path length (binary) [85]	0.75	0.75
Characteristic path length (weighted) [86]	2.1×10^{-3}	4.1×10^{-3}
Modularity [87]	$0.49 \pm (1.6 \times 10^{-4})$	$0.021 \pm (2.5 \times 10^{-5})$
Coreness [88]	0.37	0.22

- [1] D. S. Bassett and O. Sporns, Nat. Neurosci. 20, 353 (2017).
- [2] M. Breakspear, Nat. Neurosci. **20**, 340 (2017).
- [3] K. Bansal, J. Nakuci, and S. F. Muldoon, Curr. Opin. Neurobiol. 52, 42 (2018).
- [4] T. Proix, F. Bartolomei, M. Guye, and V. K. Jirsa, Brain 140, 641 (2017).
- [5] M. I. Falcon, V. Jirsa, and A. Solodkin, Curr. Opin. Neurobiol. 29, 429 (2016).
- [6] M. Schirner, S. Rothmeier, V. K. Jirsa, A. R. McIntosh, and P. Ritter, Neuroimage 117, 343 (2015).
- [7] D. S. Bassett, P. Zurn, and J. I. Gold, Nat. Rev. Neurosci. 19, 566 (2018).
- [8] M. Breakspear and C. J. Stam, Philos. Trans. R. Soc. London B 360, 1051 (2005).
- [9] R. F. Betzel and D. S. Bassett, Neuroimage **160**, 73
- [10] K. J. Friston, Annu. Rev. Physiol. **56**, 57 (2005).
- [11] K. Friston, PLoS Comput. Biol. 4, e1000211 (2008).
- [12] G. Deco, V. K. Jirsa, P. A. Robinson, M. Breakspear, and K. Friston, PLoS Comput. Biol. 4, e1000092 (2008).

- [13] C. J. Honey, O. Sporns, L. Cammoun, X. Gigandet, J. P. Thiran, R. Meuli, and P. Hagmann, Proc. Natl. Acad. Sci. USA 106, 2035 (2009).
- [14] R. Fernández Galán, PLoS One 3, e2148 (2008).
- [15] A. Raj, A. Kuceyeski, and M. Weiner, Neuron 73, 1204 (2012).
- [16] K. M. Aquino, M. M. Schira, P. A. Robinson, P. M. Drysdale, and M. Breakspear, PLoS Comput. Biol. 8, 3 (2012).
- [17] J. Viventi, D.-H. Kim, L. Vigeland, E. S. Frechette, J. A. Blanco, Y.-S. Kim, A. E. Avrin, V. R. Tiruvadi, S.-W. Hwang, A. C. Vanleer, D. F. Wulsin, K. Davis, C. E. Gelber, L. Palmer, J. Van der Spiegel, J. Wu, J. Xiao, Y. Huang, D. Contreras, J. A. Rogers, and B. Litt, Nat. Neurosci. 14, 1599 (2011).
- [18] N. J. Kopell, H. J. Gritton, M. A. Whittington, and M. A. Kramer, Neuron 83, 1319 (2014).
- [19] P. Fries, Neuron 88, 220 (2015).
- [20] A. Palmigiano, T. Geisel, F. Wolf, and D. Battaglia, Nat. Neurosci. 20, 1014 (2017).
- [21] C. Kirst, M. Timme, and D. Battaglia, Nat. Commun. 7, 11061 (2016).
- [22] L. Muller, F. Chavane, J. Reynolds, and T. J. Sejnowski, Nat. Rev. Neurosci. 19, 255 (2018), review Article.
- [23] S. Heitmann, T. Boonstra, and M. Breakspear, PLoS Comput. Biol. 9, 1 (2013).
- [24] X. Huang, W. Xu, J. Liang, K. Takagaki, X. Gao, and J. young Wu, Neuron 68, 978 (2010).
- [25] J. Stiso and D. S. Bassett, Trends Cogn. Sci. 22, 1127 (2018).
- [26] R. Chaudhuri, K. Knoblauch, M.-A. Gariel, H. Kennedy, and X.-J. Wang, Neuron 88, 419 (2015).
- [27] A. Cancelli, C. Cottone, F. Tecchio, D. Q. Truong, J. Dmochowski, and M. Bikson, J. Neural Eng. 13, 036022 (2016).
- [28] S. Lopes, N. Davies, C. Toumazou, and N. Grossman, in Proceedings of the Annual International Conference of the IEEE Engineering in Medicine and Biology Society (IEEE, Piscataway, NJ, 2012), pp. 4152–4155.
- [29] M. K. Metwally, Y. S. Cho, H. J. Park, and T. S. Kim, in Proceedings of the Annual International Conference of the IEEE Engineering in Medicine and Biology Society (IEEE, Piscataway, NJ, 2012), pp. 5514–5517.
- [30] A. Raj, E. LoCastro, A. Kuceyeski, D. Tosun, N. Relkin, and M. Weiner, Cell Rep. 10, 359 (2015).
- [31] S. R. Jones, Curr. Opin. Neurobiol. 40, 72 (2016).
- [32] M. D. Sacchet, R. A. LaPlante, Q. Wan, D. L. Pritchett, A. K. Lee, M. Hamalainen, C. I. Moore, C. E. Kerr, and S. R. Jones, J. Neurosci. 35, 2074 (2015).
- [33] A. von Stein, P. Rappelsberger, J. Sarnthein, and H. Petsche, Cereb. Cortex **9**, 137 (1999).
- [34] N. Kopell, G. B. Ermentrout, M. A. Whittington, and R. D. Traub, Proc. Natl. Acad. Sci. USA 97, 1867 (2000), retrieved from http://www.pnas.org/content/97/4/1867.full.pdf.
- [35] M. A. Sherman, S. Lee, R. Law, S. Haegens, C. A. Thorn, M. S. Hamalainen, C. I. Moore, and S. R. Jones, Proc. Natl. Acad. Sci. USA 113, E4885 (2016).
- [36] S. Lee and S. R. Jones, Front. Hum. Neurosci. 7, 869 (2013).
- [37] S. F. Muldoon, F. Pasqualetti, S. Gu, M. Cieslak, S. T. Grafton, J. M. Vettel, and D. S. Bassett, PLoS Comput. Biol. 12, e1005076 (2016).
- [38] L. M. Pecora and T. L. Carroll, Phys. Rev. Lett. 80, 2109 (1998).

- [39] E. Tang, C. Giusti, G. L. Baum, S. Gu, E. Pollock, A. E. Kahn, D. R. Roalf, T. M. Moore, K. Ruparel, R. C. Gur, R. E. Gur, T. D. Satterthwaite, and D. S. Bassett, Nat. Commun. 8, 1252 (2017).
- [40] E. Tang and D. S. Bassett, Rev. Mod. Phys. 90, 031003 (2018).
- [41] S. Gu, F. Pasqualetti, M. Cieslak, Q. K. Telesford, B. Y. Alfred, A. E. Kahn, J. D. Medaglia, J. M. Vettel, M. B. Miller, S. T. Grafton *et al.*, Nat. Commun. 6, 8414 (2015).
- [42] P. N. Taylor, J. Thomas, N. Sinha, J. Dauwels, M. Kaiser, T. Thesen, and J. Ruths, Front. Neurosci. 9, 202 (2015).
- [43] G. Yan, P. E. Vértes, E. K. Towlson, Y. L. Chew, D. S. Walker, W. R. Schafer, and A.-L. Barabási, Nature 550, 519 (2017).
- [44] J. Z. Kim, J. M. Soffer, A. E. Kahn, J. M. Vettel, F. Pasqualetti, and D. S. Bassett, Nat. Phys. 14, 91 (2018).
- [45] F. Pasqualetti, S. Zampieri, and F. Bullo, IEEE Trans. Control Netw. Syst. 1, 40 (2014).
- [46] E. J. Cornblath, E. Tang, G. L. Baum, T. M. Moore, A. Adebimpe, D. R. Roalf, R. C. Gur, R. E. Gur, F. Pasqualetti, T. D. Satterthwaite, and D. S. Bassett, Neuroimage 188, 122 (2018).
- [47] J. Jeganathan, A. Perry, D. S. Bassett, G. Roberts, P. B. Mitchell, and M. Breakspear, Neuroimage Clin. 19, 71 (2018).
- [48] A. E. Motter, Chaos 25, 097621 (2015).
- [49] Y.-Y. Liu and A.-L. Barabási, Rev. Mod. Phys. 88, 035006 (2016).
- [50] T. D. Satterthwaite, J. J. Connolly, K. Ruparel, M. E. Calkins, C. Jackson, M. A. Elliott, D. R. Roalf, K. P. Ryan Hopsona, M. Behr, H. Qiu, F. D. Mentch, R. Chiavacci, P. M. Sleiman, R. C. Gur, H. Hakonarson, and R. E. Gur, Neuroimage 124, 1115 (2016).
- [51] M. E. Calkins, K. R. Merikangas, T. M. Moore, M. Burstein, M. A. Behr, T. D. Satterthwaite, K. Ruparel, D. H. Wolf, D. R. Roalf, F. D. Mentch, H. Qiu, R. Chiavacci, J. J. Connolly, P. M. A. Sleiman, R. C. Gur, H. Hakonarson, and R. E. Gur, J. Child Psychol. Psychiatry 56, 1356 (2015).
- [52] S. Atasoy, I. Donnelly, and J. Pearson, Nat. Commun. 7, 10340 (2016), article.
- [53] Z. He, X. Wang, G.-Y. Zhang, and M. Zhan, Phys. Rev. E 90, 012909 (2014).
- [54] G. L. Baum, R. Ciric, D. R. Roalf, R. F. Betzel, T. M. Moore, R. T. Shinohara, A. E. Kahn, S. N. Vandekar, P. E. Rupert, M. Quarmley, P. A. Cook, M. A. Elliott, K. Ruparel, R. E. Gur, R. C. Gur, D. S. Bassett, and T. D. Satterthwaite, Curr. Biol. 27, 1561 (2017).
- [55] G. L. Baum, D. R. Roalf, P. A. Cook, R. Ciric, A. F. G. Rosen, C. Xia, M. A. Elliott, K. Ruparel, R. Verma, B. Tunc, R. C. Gur, R. E. Gur, D. S. Bassett, and T. D. Satterthwaite, Neuroimage 173, 275 (2018).
- [56] R. E. Kalman, Y. C. Ho, and K. S. Narendra, Contrib. Differ. Equat. 1, 189 (1963).
- [57] T. Kailath, *Linear Systems*, Vol. 1 (Prentice-Hall, Englewood Cliffs, NJ, 1980).
- [58] G. Hewer and C. Kenney, SIAM J. Control Optim. 26, 321 (1988).
- [59] P. M. Gahinet, A. J. Laub, C. S. Kenney, and G. A. Hewer, IEEE Trans. Autom. Control 35, 1209 (1990).
- [60] S. J. Hammarling, IMA J. Numer. Anal. 2, 303 (1982).
- [61] D. C. Sorensen and Y. Zhou, Bounds on eigenvalue decay rates and sensitivity of solutions to Lyapunov equations, Technical Report No. TR02-07, Rice University, Texas, 2002.

- [62] E. Wu-Yan, R. F. Betzel, E. Tang, S. Gu, F. Pasqualetti, and D. S. Bassett J. Nonlinear Sci. (2018), doi: 10.1007/s00332-018-9448-z.
- [63] J. A. Roberts, L. L. Gollo, R. G. Abeysuriya, G. Roberts, P. B. Mitchell, M. W. Woolrich, and M. Breakspear, Nat. Commun. 10, 1056 (2019).
- [64] D. S. Bassett and E. T. Bullmore, Neuroscientist. 23, 499 (2017)
- [65] D. S. Bassett and E. Bullmore, Neuroscientist 12, 512 (2006).
- [66] R. F. Betzel, J. D. Medaglia, and D. S. Bassett, Nat. Commun. 9, 346 (2018).
- [67] R. Albert and A.-L. Barabasi, Rev. Mod. Phys. 74, 47 (2002).
- [68] D. J. d. S. Price, J. Am. Soc. Inf. Sci. 27, 292 (1976).
- [69] A. L. Barabasi and R. Albert, Science 286, 509 (1999).
- [70] M. Porfiri, Europhys. Lett. 96, 40014 (2011).
- [71] J. Sun, E. M. Bollt, and T. Nishikawa, Europhys. Lett. 85, 60011 (2009).
- [72] J. Jiang and Y.-C. Lai, Nat. Commun. 10, 3961 (2019).
- [73] L. Huang, Q. Chen, Y.-C. Lai, and L. M. Pecora, Phys. Rev. E 80, 036204 (2009).
- [74] C. Tu, R. P. Rocha, M. Corbetta, S. Zampieri, M. Zorzi, and S. Suweis, Neuroimage 176, 83 (2018).
- [75] F. Pasqualetti, S. Gu, and D. S. Bassett, Neuroimage 197, 586 (2019)
- [76] T. Menara, S. Gu, D. S. Bassett, and F. Pasqualetti, in *IEEE Transactions on Automatic Control* (IEEE, 2019), Vol. 64, pp. 3740–3747.
- [77] J. G. T. Zañudo, G. Yang, and R. Albert, Proc. Natl. Acad. Sci. USA 114, 7234 (2017).

- [78] S. Gu, R. F. Betzel, M. G. Mattar, M. Cieslak, P. R. Delio, S. T. Grafton, F. Pasqualetti, and D. S. Bassett, Neuroimage 148, 305 (2017).
- [79] R. F. Betzel, S. Gu, J. D. Medaglia, F. Pasqualetti, and D. S. Bassett, Sci. Rep. 6, 30770 (2016).
- [80] J. Stiso, A. N. Khambhati, T. Menara, A. E. Kahn, J. M. Stein, S. R. Das, R. Gorniak, J. Tracy, B. Litt, K. A. Davis, F. Pasqualetti, T. H. Lucas, and D. S. Bassett, Cell Rep. 28, 2554 (2019).
- [81] Z. Cui, J. Stiso, G. L. Baum, J. Z. Kim, D. R. Roalf, R. F. Betzel, S. Gu, Z. Lu, C. H. Xia, X. He, R. Ciric, D. J. Oathes, T. M. Moore, R. T. Shinohara, K. Ruparel, C. Davatzikos, F. Pasqualetti, R. E. Gur, R. C. Gur, D. S. Bassett, and T. D. Satterthwaite, eLife 9, e53060 (2020).
- [82] D. R. Roalf, M. Quarmley, M. A. Elliott, T. D. Satterthwaite, S. N. Vandekar, K. Ruparel, E. D. Gennatas, M. E. Calkins, T. M. Moore, R. Hopson, K. Prabhakaran, C. T. Jackson, R. Verma, H. Hakonarson, R. C. Gur, and R. E. Gur, NeuroImage 125, 903 (2016).
- [83] S. N. Vandekar, R. T. Shinohara, A. Raznahan, D. R. Roalf, M. Ross, N. DeLeo, K. Ruparel, R. Verma, D. H. Wolf, R. C. Gur, R. E. Gur, and T. D. Satterthwaite, J. Neurosci. 35, 599 (2015).
- [84] A. Daducci, S. Gerhard, A. Griffa, A. Lemkaddem, L. Cammoun, X. Gigandet, R. Meuli, P. Hagmann, and J.-P. Thiran, PLoS One 7, 1 (2012).
- [85] D. J. Watts and S. H. Strogatz, Nature 393, 440 (1998).
- [86] M. Rubinov and O. Sporns, Neuroimage 52, 1059 (2010).
- [87] M. E. J. Newman, Phys. Rev. E 69, 066133 (2004).
- [88] S. P. Borgatti and M. G. Everett, Social Netw. 21, 375 (2000).